Electronic Supplement for Article:

'Automatic S-Wave Picker for Local Earthquake Tomography' by T. Diehl, N. Deichmann, E. Kissling and S. Husen

A Character of S-Waves at Local Distances

The nature of shear waves and their interaction with the medium they have travelled through must be taken into account for visual as well as for automatic determination of S-wave arrival times. If $\vec{L}$ defines the direction of propagation of the compressional P-wave, the particle motion of the S-wave is confined to a plane perpendicular to $\vec{L}$. The particle motion within this plane can be described by two normal vectors: the horizontal component (SH) and the vertical component (SV). Furthermore, in an isotropic medium the particle motion of P and S body waves is assumed to be linearly polarized.

The correct picking and identification of the first arriving S-phase can be complicated by various factors. As a later arriving phase, it can be superposed by the P coda and is sometimes preceded by later arriving P phases like the PmP reflection from the Moho (Fig. S1). Due to the coupling between P and SV, velocity interfaces cause conversion of SV to P energy (and vice versa) as demonstrated in Figure S1. Such converted Sp precursors generated at interfaces close to the surface (e.g., at the basement/sediment boundary) can be misinterpreted as the first S-onset (see also *Thurber and Atre*, 1993).

Beyond the crossover distance the Sn phase refracted at the Moho is expected to be the first arriving S-phase. Usually, this phase is rather emergent and small in amplitude compared to later arriving S-phases like Sg or SmS. Even in synthetic seismograms of Figure S1 the Sn phase is difficult to identify, and on R and Z component it is not visible at all. Therefore, it is likely to be missed in real data.

At larger distances, especially for shallow focal depths, the linear polarization of the Sg phase gradually changes to elliptical polarization (transition to Lg phase), and the corresponding onset becomes more emergent. In addition, seismic anisotropy reduces the degree of linear polarization and leads to splitting of the shear waves (for a review see e.g., *Crampin and Lovell*, 1991; *Weiss et al.*, 1999).

The identification of first-arrival S-waves and its picking accuracy can be improved by applying various signal processing techniques. Rotation of components represents a common procedure to enhance the S-wave onset (see e.g., *Plešinger et al.*, 1986). S-waves can also be identified by polarization analysis. Common tools are particle motion diagrams and polarization filters, which e.g., enhance linearly polarized body waves. Finally, appropriate waveform

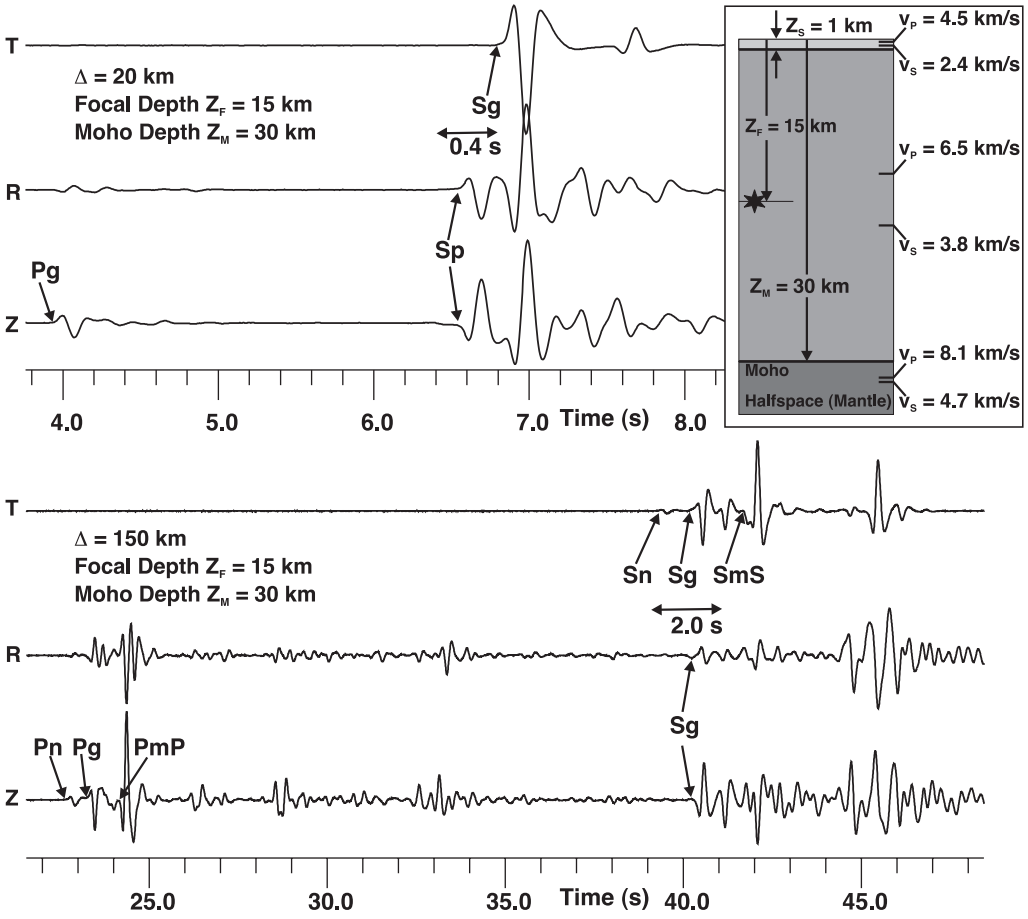

Figure S1: Reflectivity seismograms (*Fuchs and Müller*, 1971) for a simplified 1-D crustal model (upper right inset). Uppermost layer represents a sedimentary basin of reduced P- and S-wave velocities. The uppermost traces show vertical, radial and transverse component at a distance of 20 km. The Sp precursor phase is clearly visible on Z and R component. Lowermost traces correspond to a distance of 150 km. The amplitude of the first arriving Sn phase is rather weak compared to later-arrivals (Sg, SmS) and only visible on the T component. All amplitudes are normalized by station maximum. Seismograms were calculated using the $refmet$ code provided by T. Forbriger.

filters, like the Wood-Anderson filter, which essentially integrates the signal, can enhance the low-frequency character of S-waves.

B Combined Picking Approach (Supplementary Material)

In this section we provide a detailed description of the STA/LTA-detector, the polarization detector, the AR-AIC picker, and the automatic quality assessment. This detailed documentation is intended for any potential user who wants to reproduce our approach (or parts of it). It represents an important complement to the paper 'Automatic S-wave picker for local earthquake tomography' of Diehl et al. 2008.
In the following sections we consider a three component time series (Z,N,E) of N samples with a sampling interval of Δt. The corresponding amplitudes are represented by y_{ji}, with $j = 1, 2, 3$ and $i = 1, N$. To facilitate the reader's orientation, variables used in the description of detectors and picker are summarized in the glossary of Table S1.

B.1 STA/LTA Detector

In our STA/LTA implementation, we calculate the short-term average for the ith sample in a window of length s samples from $i - s$ to i:

$$STA_{ji} = \frac{1}{s+1} \sum_{i-s}^{i} {y_{ji}}^2 \tag{S1}$$

The long-term average is calculated in an analogous way over a window of length l samples:

$$LTA_{ji} = \frac{1}{l+1} \sum_{i-l}^{i} {y_{ji}}^2 \tag{S2}$$

We define the combined horizontal STA/LTA ratio, HSL, for the N and E-component as:

$$HSL_i = \frac{STA_{2i}}{LTA_{2i}} \cdot \frac{STA_{3i}}{LTA_{3i}} \tag{S3}$$

Several short-term (Δst) and long-term (Δlt) window lengths were tested for our data set. For the Alpine region, a combination of $\Delta st = 0.20$ s and $\Delta lt = 2.00$ s yields the best compromise between hit rate and false detections. To restrict the detection to possible S-phases, we have to ensure that no P-wave is present in the S-detection window. The proposed setup of the S-phase search windows assumes that, on the horizontal components, the S-arrival is

Variable	Description
General Variables	
tP_{obs}	Time of *a priori* (known) P-arrival (e.g., from high-quality autopick)
tS_{pre}	Time of predicted S-arrival (e.g., from velocity model)
t_{MHA}	Time of Maximum Horizontal Amplitude y_{MHA}
$SW1$, $SW2$	Time of start and end of S-picking window for both detectors
tS_{me}	Time of final automatic S-pick (from quality assessment)
tS_{up}	Time of upper end of error interval (from quality assessment)
tS_{lo}	Time of lower end of error interval (from quality assessment)
Variables used for STA/LTA Detector	
$tS2L_{max}$	Time of maximum STA/LTA value $S2L_{max}$
thr_1	Dynamic threshold for STA/LTA detector
tS_{thr1}	Time of threshold-based STA/LTA S-pick ('latest possible')
tS_{min1}	Time of minimum-based STA/LTA S-pick ('earliest possible')
Variables used for Polarization Detector	
t_3	Time of end of window for threshold determination (start: $SW1$)
thr_2	Dynamic threshold for polarization detector
tS_{thr2}	Time of threshold-based polarization S-pick ('latest possible')
tS_{min2}	Time of minimum-based polarization S-pick ('earliest possible')
Variables used for AR-AIC Picker	
t_{AC}	Time of initial pick for AIC configuration (from detectors or tS_{pre})
t_{NS}, t_{NE}	Time of start and end of noise model window
t_{SS}, t_{SE}	Time of start and end of signal model window
AIC^C	AIC function for component C (C=N, E, T, Q, or H); H=E+N
tS_{AC}	Time of AIC-minium for component C (C=N, E, T, Q, or H)
thr_{AIC}	Dynamic threshold for AIC quality assessment
tS_{eC}	Time of 'earliest possible' AIC-pick for component C
tS_{lC}	Time of 'latest possible' AIC-pick for component C
Variables used for Quality Assessment	
tS_{av}	Average time of all considered picks
σ_{pk}	Standard deviation of all considered picks
tS_{er}	Earliest time of all considered picks
tS_{la}	Latest time of all considered picks

Table S1: Complete glossary of variables used and returned by the different detectors and pickers.

located prior and close to the largest amplitude. To minimize the effect of inaccurately predicted S-arrivals, tS_{pre}, we use this information only for the definition of a first coarse window starting at $tP_{obs} + (tS_{pre} - tP_{obs})/4$ and ending at $tS_{pre} + \Delta S_{post}$. In case of early predicted S-arrival times, ΔS_{post} has to ensure that the dominant part of the S-wave coda is still included in the coarse search window. The choice of ΔS_{post} depends on the largest possible deviation expected between the predicted S and the actual S-arrival (mainly related to the accuracy of the velocity model and the hypocenter). In our data set a value of 5.0 s seems sufficient.
The coarse S-window is used to determine the position of the maximum horizontal amplitude y_{MHA} at time t_{MHA} as illustrated in Figure S2. We ex-

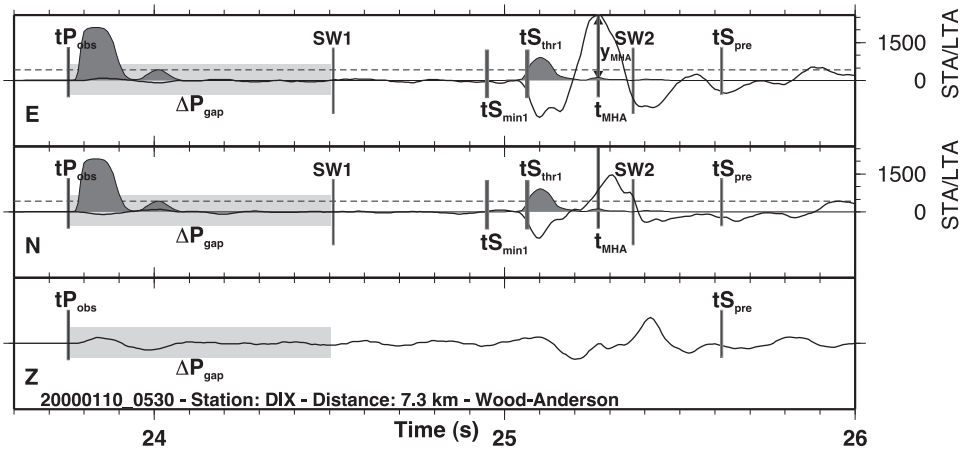

Figure S2: Combined STA/LTA approach used for S-wave detection on horizontal components. Black solid lines represent the Wood-Anderson filtered 3C seismograms (amplitudes normalized by station maximum) of a local earthquake in Switzerland (M_l=3.1, focal depth of 9 km). The dark gray shaded trace denotes the combined STA/LTA ratio derived from N and E components. tP_{obs} represents the known P-arrival time and tS_{pre} indicates the position of theoretical S-arrival predicted from a regional 1-D model. The dashed horizontal line denotes the dynamic threshold thr_1 for the picking algorithm. The S-wave arrival time based on the STA/LTA detector in the potential S-window ($SW1$ to $SW2$) is most likely located in the interval between tS_{min1} (minimum pick) and tS_{thr1} (threshold pick). See text and Table 1 for further description.

pect the actual S-phase onset to certainly occur prior to t_{MHA} and therefore, $t_{MHA} + (2 \cdot tup)$ defines the upper end of the search window ($SW2$ in Fig. S2). The additional term $2 \cdot tup$ is required for the picking algorithm, which will be described later. The start of the S-window is derived from $tP_{obs} + (t_{MHA} - tP_{obs})/2$ and is indicated as $SW1$ in Figure S2. For very short epicentral distances, it is still possible that the search window from $SW1$ to $SW2$ includes parts of the P-signal. Therefore, a fixed minimum safety gap ΔP_{gap} is required between tP_{obs} and $SW1$ (represented by light gray band in Fig. S2). If $SW1$ falls within this safety gap, it is automatically adjusted to $tP_{obs} + \Delta P_{gap}$. We set $\Delta P_{gap} = 0.75$ s.
The picking algorithm applied to the characteristic STA/LTA function within

the search window is similar to the method proposed by *Baer and Kradolfer* (1987). We extended their threshold-based method by a 'minimum-picking' approach also suggested by *Cichowicz* (1993), where a (global) minimum of the characteristic function (CF) prior to the threshold-based pick is determined. The iterative application of threshold and minimum-picking techniques provides a direct assessment of the uncertainty of the phase arrival and is closely related to procedures used in manual picking. Instead of adopting a fixed STA/LTA-threshold, we determine the threshold-value thr_1 from the standard deviation σ_1 of the STA/LTA function within the search window. If $S2L_{max}$ denotes the maximum STA/LTA value within the search window, thr_1 is defined by:

$$thr_1 = \begin{cases} 2 \cdot \sigma_1 & : \quad \sigma_1 < S2L_{max}/2 \\ S2L_{max}/2 & : \quad \sigma_1 \geq S2L_{max}/2 \end{cases} \tag{S4}$$

The dashed horizontal lines in Figure S2 represent thr_1 for our example. A pick is declared if the actual STA/LTA exceeds the threshold thr_1 and remains above the threshold for a minimum time *tup*. For very impulsive S-waves, we have to ensure that *tup* can be reached within the picking window. Therefore, $SW2$ is defined as $t_{MHA} + (2 \cdot tup)$. To account for roughness and singularities present in characteristic functions derived from complex seismic signals, *Baer and Kradolfer* (1987) introduced the additional parameter *tdw*. The pick flag is not cleared if the CF drops below the threshold for a time interval less than *tdw*. We obtained stable results for $tup = 0.05$ s and, due to the usually rather smooth STA/LTA function, we set *tdw* to zero. The corresponding threshold-based pick in Figure S2 is represented by tS_{thr1}.
Our 'minimum-picking' approach determines the minimum value of the CF prior to tS_{thr1} and is equivalent to a delay correction usually necessary for threshold-based picks. This minimum can be interpreted as the position of the earliest possible arrival time of the phase detected by the threshold method. To account for local minima and to include possible smaller precursory phases, we introduce an parameter *tbe* similar to *tup*. If a minimum prior to tS_{thr1} is detected, we require that the values of the CF remain below $thr_1/2$ for the period of *tbe* backward in time. The corresponding 'minimum' pick is represented by tS_{min1} in Figure S2. For the STA/LTA detector, we use $tbe = tup$.

B.2 Polarization Detector

The implementation of our polarization detector is mainly based on the approach of *Cichowicz* (1993) and its principles are described in the following paragraph.
As a first step, we determine the direction of the incoming P-wave. We compute the three-component covariance matrix within a narrow window of length ΔwP around the known first arriving P-phase tP_{obs}. The eigenvector corre-

sponding to the maximum eigenvalue of the covariance matrix represents the direction of the P-wave $\vec{L}$. The direction in the reference observation system (ZEN) can be defined by two angles, the back-azimuth β and the angle of incidence φ. The window length used to calculate the covariance matrix is a critical parameter in this procedure, since it can have a significant influence on uncertainty and reliability of the derived rotation angles. In the presence of multiple arrivals or scattered phases close to the first-arrival, long windows can lead to unstable results. On the other hand, very narrow windows can result in wrong rotation angles if the onset of the analyzed wavelet is emergent. To account for differences in the wavelet characteristics, we simply weight the window length by the *a priori* observation quality of the P-phase. Table S2 describes the weighting scheme used for P-phase picking in the Alpine region (*Diehl et al.*, 2009). The window length used to analyze a P-phase of quality

P-Quality class qP	Error ε_{qP} (s)	Weight (%)
0	$\pm$ 0.05	100
1	$\pm$ 0.10	50
2	$\pm$ 0.20	25
3	$\pm$ 0.40	12.5
4	$>$ 0.40	0 (rejected, not considered)

Table S2: Weight assignments based on picking errors for P-waves from local and regional earthquakes within the greater Alpine region (*Diehl et al.*, 2009).

class qP is:

$$\Delta wP = 2 \cdot \varepsilon_{qP}, \tag{S5}$$

where ε_{qP} denotes the error interval associated with quality class qP. To separate P from SV and SH-energy, we rotate the observation system (ZEN) into a ray-coordinate system (LQT) using rotation angles β and φ according to *Plešinger et al.* (1986):

$$\begin{pmatrix} L \\ Q \\ T \end{pmatrix} = \begin{pmatrix} \cos\varphi & -\sin\varphi\sin\beta & -\sin\varphi\cos\beta \\ \sin\varphi & \cos\varphi\sin\beta & \cos\varphi\cos\beta \\ 0 & -\cos\beta & \sin\beta \end{pmatrix} \begin{pmatrix} Z \\ E \\ N \end{pmatrix} \tag{S6}$$

Finally, we calculate the directivity $D(t)$, rectilinearity $P(t)$, ratio between transverse and total energy $H(t)$, and a weighting factor $W(t)$ within a centered window of length Δpol for each sample of the rotated time series. The length of the polarization filter Δpol used to analyze a seismogram with a given P-phase of quality class qP is derived from the following expression:

$$\Delta pol = 4 \cdot \varepsilon_{qP} \tag{S7}$$

Again, we account for differences in waveform characteristics by weighting the length of the polarization filter with the P-phase quality. The covariance matrix is determined from the centered window for each sample.
Directivity $D(t)$ is defined as the normalized angle between $\vec{L}$ and eigenvector $\vec{\epsilon}_{max}$ corresponding to the maximum eigenvalue of the covariance matrix. The directivity operator is expected to be close to zero for the first arriving P-wave ($\vec{\epsilon}_{max}$ parallel to $\vec{L}$) and close to one for the first arriving S-wave ($\vec{\epsilon}_{max}$ perpendicular to $\vec{L}$).
Rectilinearity $P(t)$ is calculated using the formulation of *Samson* (1977):

$$P(t) = \frac{(\lambda_1 - \lambda_2)^2 + (\lambda_1 - \lambda_3)^2 + (\lambda_2 - \lambda_3)^2}{2 \cdot (\lambda_1 + \lambda_2 + \lambda_3)^2}, \tag{S8}$$

where λ_1, λ_2, λ_3 are the eigenvalues of the covariance matrix at time t. $P(t)$ is expected to be close to one for both first arriving P- and S-waves.
The ratio between transverse and total energy $H(t)$ within the centered window is defined as

$$H(t) = \frac{\sum\limits_j ({Q_j}^2 + {T_j}^2)}{\sum\limits_j ({Q_j}^2 + {T_j}^2 + {L_j}^2)}. \tag{S9}$$

Likewise, $H(t)$ is expected to be close to one for the first arriving S-wave and zero for the first arriving P-wave.
As an addition to the original method of *Cichowicz* (1993), we calculate a weighting factor $W(t)$ for each window, which accounts for the absolute amplitude within the centered window with respect to the maximum amplitude derived from the coarse S-window:

$$W(t) = \left(\frac{y_{mwin}}{y_{MTA}}\right)^n \tag{S10}$$

Here, y_{mwin} denotes the maximum transverse amplitude within the centered window and y_{MTA} represents the maximum transverse amplitude in the coarse S-window (determined on Q and T similarly to y_{MHA}). The exponent n increases ($n > 0$) or decreases ($n < 0$) the weighting effect. The usage of such a weighting factor significantly reduces the noise of the CF prior to the S-wave arrival. We obtained the best results for $n = 0.5$.
The product of the three squared filter operators $D(t)$, $P(t)$, $H(t)$ with the weighting factor $W(t)$ yields the modified characteristic function for S-wave detection CF_S:

$$CF_S(t) = D^2(t) \cdot P^2(t) \cdot H^2(t) \cdot W(t) \tag{S11}$$

Figure S3 shows the LQT components of the same local earthquake from Figure S2 and the corresponding S-wave operators $D(t)$, $P(t)$, and $H(t)$. The arrival

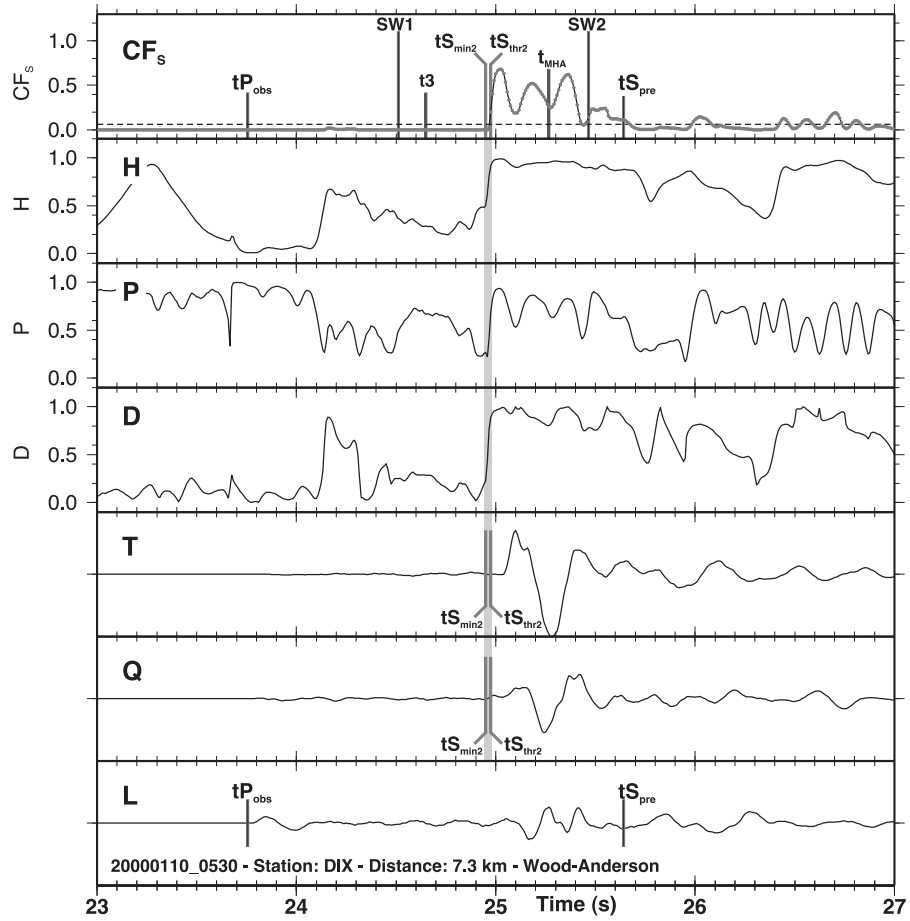

Figure S3: Example for the polarization detector applied to the same local earthquake of Figure S2. L, Q, T denote the rotated components. The corresponding S-wave operators are $D(t)$ (directivity), $P(t)$ (rectilinearity), and $H(t)$ (transverse to total energy ratio). The uppermost trace represents the amplitude weighted characteristic S-wave function CF_s and the dashed horizontal line denotes the dynamic threshold thr_2 for the picking algorithm. The arrival of the S-wave (gray band) goes along with the simultaneous increase of $D(t)$, $P(t)$, $H(t)$, and CF_S. Compared to the actual arrival on T, the S-wave detection is shifted by approximate 0.1 s to earlier times. This time-shift is caused by the finite length of the polarization filter. CF_S is not affected by the P-wave. See text and Tables S1 for further description.

of the S-wave (gray band) goes along with the simultaneous increase of $D(t)$, $P(t)$, and $H(t)$ and leads to a well-defined signature on CF_S.
The picking algorithm applied to CF_S is almost identical to the one used for the STA/LTA detector described above. The S-wave search window starts at $SW1 = tP_{obs} + (t_{MHA} - tP_{obs})/2$ and ends at $SW2 = t_{MHA} + (2 \cdot tup)$, where tup can deviate from the value used for the STA/LTA detector. The threshold thr_2 for the picker (dashed horizontal line in Figure S3) is derived from the standard deviation σ_2 and the mean $\overline{CF_S}$ of CF_S between $SW1$ and $t3$ according to the procedure proposed by *Cichowicz* (1993). The position of $t3$ is defined as $SW1 + (t_{MHA} - SW1 - \Delta pol)/4$ and the threshold is calculated from:

$$thr_2 = \overline{CF_S} + (3 \cdot \sigma_2) + cw, \tag{S12}$$

where cw denotes a 'water-level', which stabilizes the picking in case of a large signal-to-noise ratio. Otherwise, thr_2 would approach zero, since σ_2 as well as $\overline{CF_S}$ become small for large signal-to-noise ratios. We use $cw = 0.06$, $tup = 0.10$ s, and $tdw = 0.05$ s for the threshold-based picking on CF_S and the corresponding pick is represented by tS_{thr2} in Figure S3. In addition, we perform the minimum-picking prior to tS_{thr2} as described earlier. To account for smaller precursory signals, we choose $tbe = 2 \cdot tup$. The position of the minimum-pick is marked as tS_{min2} in Figure S3. Compared to the actual arrival on the transverse component, tS_{thr2} and tS_{min2} are shifted by approximate 0.1 s to earlier times (Fig. S3). This time-shift is caused by the finite length of the polarization filter. For emergent arrivals the time-shift is less significant.

B.3 Autoregressive Picker

Following the definition of *Takanami and Kitagawa* (1988) the time series $x_n\{n = 1, \ldots, N_A\}$ can be divided into two subseries before and after the unknown arrival time, and each of them can be expressed by an AR model:

$$x_n = \sum_{m=1}^{M(1)} a_m^1 x_{n-m} + \varepsilon_n^1, \quad (1 \leq n < n_1), \tag{S13}$$

$$x_n = \sum_{m=1}^{M(2)} a_m^2 x_{n-m} + \varepsilon_n^2, \quad (n_1 \leq n \leq N_A), \tag{S14}$$

where ε_n^i is Gaussian white noise with zero mean and variance σ_i^2, a_m^i is the autoregressive coefficient, $M(i)$ is the order of the i-th model, and n_1 corresponds to the unknown arrival time. Equation (S13) represents the background 'noise' model and Eq. (S14) the corresponding 'earthquake' model. The AIC can be considered as a measure of the deficiency of the estimated model and is given

by:

$$AIC = -2(\log L_{max}) + 2(M_P), \tag{S15}$$

where L_{max} denotes the maximum likelihood function of the two AR models and M_P is the number of independently estimated parameters. *Takanami and Kitagawa* (1988) show, that the AIC can be reduced to a function of n_1. Therefore, n_1 corresponding to the minimum AIC_{n_1} represents the best AIC estimate of the arrival time.
In practice, we calculate the noise model AIC_i^{forw} forward in time starting at t_{NS} and ending at t_{SS}, assuming the noise part is included in the window from t_{NS} to t_{NE} as illustrated in the lower box of Figure 4. In addition, the signal model AIC_i^{back} is calculated backward in time starting at t_{SE} and ending at t_{NE}, where parts of the signal are expected to be included in the window between t_{SS} and t_{SE}. By simply adding AIC_i^{forw} and AIC_i^{back} for common samples of the time series, we obtain the AIC_i of the locally stationary AR model. If i_{min} corresponds to the sample of the minimum AIC_i value, then $i_{min} + 1$ represents the best estimate of the arrival time. Moreover, AIC_i from different components can be added to give combined AIC functions, e.g. AIC^H represents the sum of the horizontal components N and E. In practice, the position and length of the noise, pick, and signal windows, as defined by t_{NS}, t_{NE}, t_{SS}, and t_{SE}, is set by an initial pick and some fixed parameters as described in the following section.

Configuration of AR-AIC Windows
Due to their fundamental concept, predictive AR-AIC pickers always require an initial pick t_{AC} to setup a noise model window ΔLN and signal model window ΔLS separated by the picking window $\Delta gN + \Delta gS$ (Fig. 4). Previous implementations of AR-AIC pickers such as *Sleeman and van Eck* (1999) or *Akazawa* (2004) mainly use triggers from STA/LTA detectors for this purpose. In our procedure, t_{AC} can be derived from the polarization detector, from the STA/LTA detector, or from a theoretical travel time. The search windows are centered around t_{AC}, and in the configuration of Figure 4, the first arriving P-wave is included in the noise window between t_{NS} and t_{NE}. The corresponding AIC functions have the typical shape with well developed minima around the actual onset of the S-wave (Fig. 4). The AR-AIC estimated picks tS_{AQ} and tS_{AT} agree very well with the arrival observed on the different components. The onset appears more impulsive on the T component, which is also indicated by the sharper minimum on AIC^T compared to the one observed on AIC^Q (Fig. 4).
The quality of AR-AIC pickers depends mainly on the degree of separation between noise and signal in the analysis window from t_{NS} to t_{SE}. This can be critical if, for example, several phases are present within the window (e.g., Pg and Sg at very short epicentral distances or Sn and Sg at larger distances). Therefore, minimum *a priori* information is required to guide the picker to

the correct phase and to setup the AR-AIC search windows properly. The examples in Figure 4, S4, and S5 are used to demonstrate the importance of correctly configured search windows for AR-AIC picking of S-wave arrivals. The configuration in Figure S4 uses the same initial pick t_{AC}. However, the picking range, noise, and signal windows are much longer than in Figure 4. With this search window configuration, part of the first arriving P-wave is included in the picking window between t_{NE} and t_{SS}. The resulting shape of the

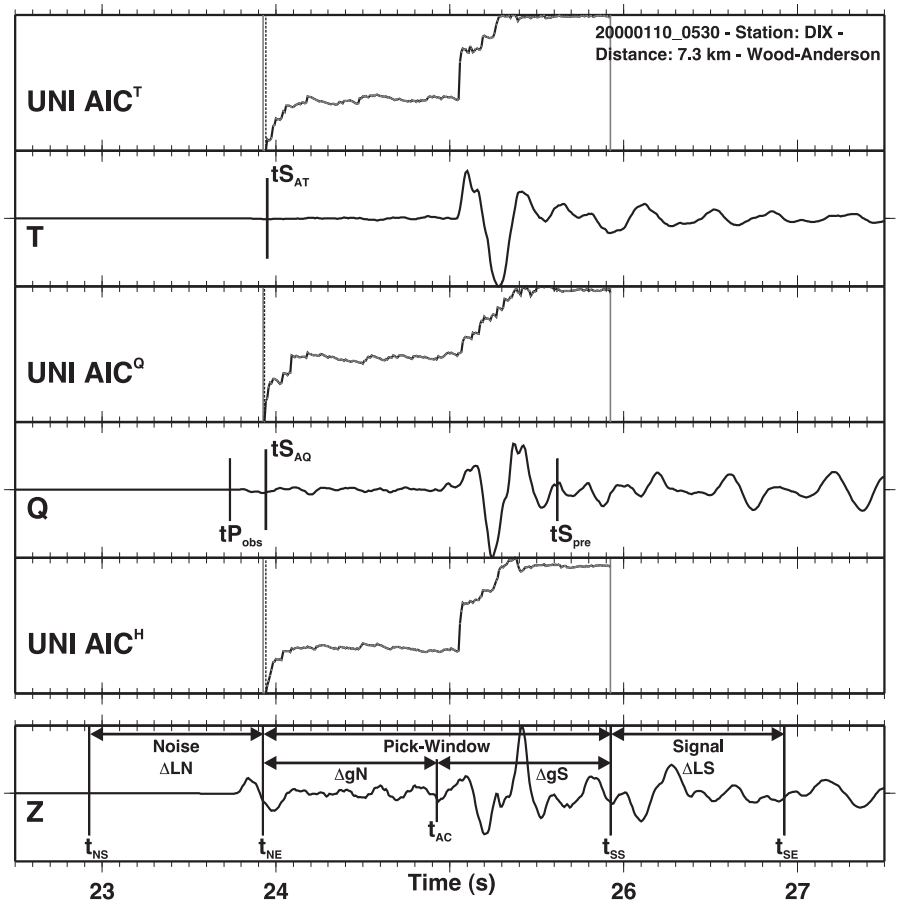

Figure S4: Example for misconfigured AR-AIC search windows (Sg case). Part of the P-wave is included in the picking window between t_{NE} and t_{SS}. This configuration leads to a deformed AIC function with the absence of a global minimum around the actual S-wave arrival. The corresponding AR-AIC picks tS_{AQ} and tS_{AT} are erroneous, being far-off the actual S-wave arrival.

AIC functions is rather unexpected and no global minimum close to the actual S-wave arrival can be observed. Consequently, the corresponding AR-AIC S-picks are grossly wrong in this example. Figure S5 illustrates a similar effect of larger epicentral distances, where a weak first-arrival Sn is followed by an impulsive and strong Sg or SmS phase. The emergent Sn phase is missed by the STA/LTA and the polarization detector (Fig. S5d). Misconfigured AR-AIC search windows as represented by configuration A in Figure S5a,b will

also fail to detect the precursor Sn phase and can result in errors up to several seconds.

Dynamic Configuration Approach

To avoid such problems, we implemented a sophisticated procedure for a dynamic configuration of AR-AIC search windows. The method used to derive the initial pick t_{AC} depends on the epicentral distance Δ_{epi}. Since theoretical travel times can deviate significantly from the actual S-wave onset due to variation in v_P/v_S or an incorrect hypocenter (in particular focal depth), t_{AC} as provided by the phase detectors is usually more reliable for stations close to the epicenter. For larger distances the effect of erroneous focal depths is less severe and the mean v_P/v_S ratio is less affected by lateral variations of the upper crust. Although the three pickers should work as independently as possible, information from the other detectors are essential for the correct setup of the AR-AIC search windows at small epicentral distances. For larger distances, the phase detectors become less reliable (e.g., smaller signal-to-noise ratio) as shown in Figure S5d, and therefore independent information from predicted arrivals in an appropriate velocity model can do a better job. The epicentral distance above which the theoretical travel time tS_{pre} is used for t_{AC} determination is defined as Δ_{AIC_1}. If present, tS_{min2} (from polarization analysis) is taken as the initial pick for distances $< \Delta_{AIC_1}$. If no phase was picked by the polarization detector, tS_{min1} (from STA/LTA) will be used for t_{AC}. In the rare case of no phase detection, tS_{pre} will be used also for small distances.

The width of the picking window centered around t_{AC} is controlled by ΔgN and ΔgS (Fig. 4). Their lengths depend mainly on the expected deviation between t_{AC} and the actual phase arrival. A wide window allows picking in case of less accurately predicted travel times, however, mispicks as demonstrated in Figure S4 and Figure S5 become more likely. The lengths of ΔLN and ΔLS depend mainly on the expected maximum wavelengths of noise and signal, respectively.

The information about the first arriving P-wave tP_{obs} is required to adjust the search windows for small epicentral distances. If $t_{NS} - tP_{obs} \leq 0$ or $t_{NE} - tP_{obs} \leq 0$ we set $\Delta LN = \Delta LS = \Delta gN = \Delta gS = (t_{AC} - tP_{obs})/2$ to ensure proper search window configuration (Fig. 4). The approximate crossover distance between Sg and Sn as first arriving S-phase is defined by Δ_{AIC_3}. As demonstrated by *Diehl et al.* (2009) for automatic P-phase picking, the first arriving phase is usually less well-defined beyond the crossover distance. Due to this change in the signal character of the first arriving phase, different picking procedures have to be used below and above the approximate crossover distance.

For distances $< \Delta_{AIC_3}$ the maximum of the STA/LTA value $tS2L_{max}$ is usually associated with the onset of the first arriving Sg phase. Possible picks derived from the STA/LTA or the polarization detector can be used for the proper

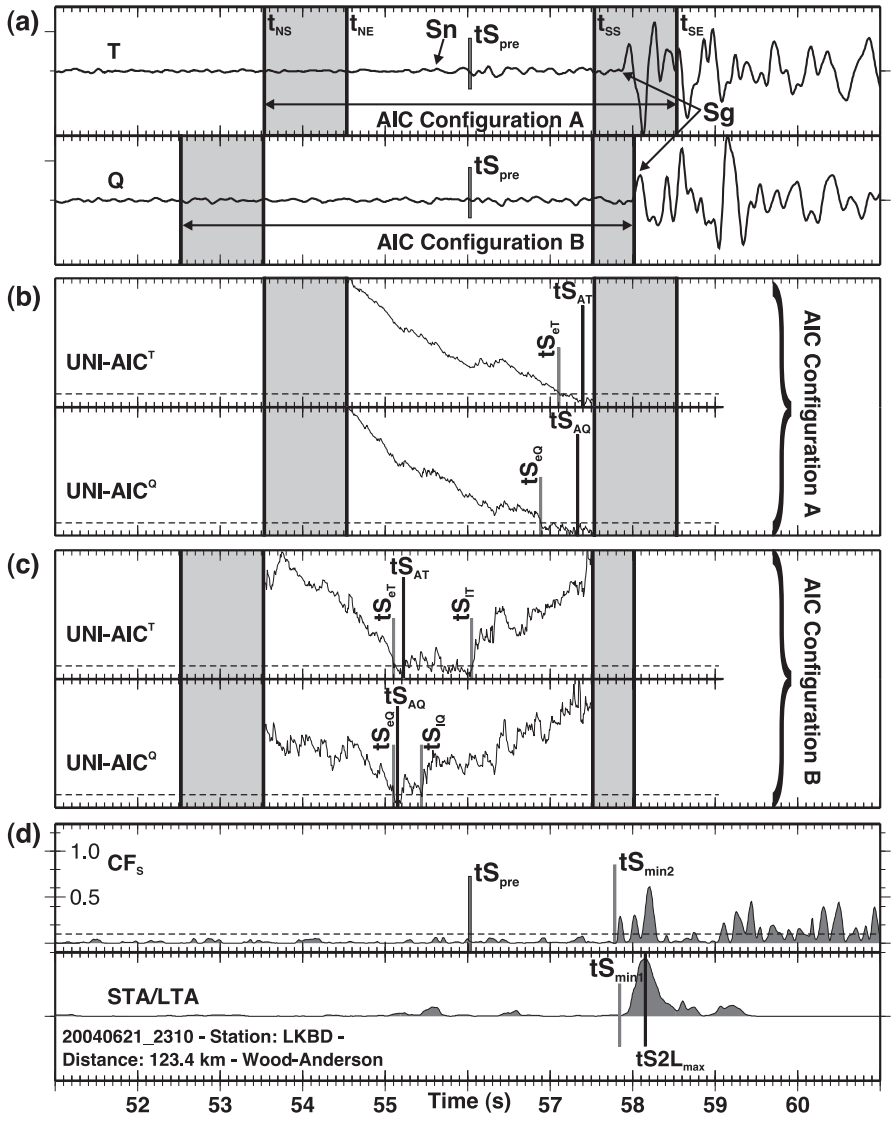

Figure S5: Example for misconfigured AR-AIC search windows (Sn case). **(a)** Major parts of the Sg-wavelet are included in the signal window between t_{SS} and t_{SE} in configuration A. **(b)** The weak emergent onset of the preceding Sn phase is missed within this static search window configuration A and the corresponding AIC functions show no distinct minimum. **(a)** By excluding the maximum of the STA/LTA function $tS2L_{max}$ from the signal window in configuration B, a proper search window configuration for Sn identification is obtained. **(c)** The flatness of the AIC-function between t_{eT} and t_{lT} represents a realistic uncertainty estimate for the weak Sn phase with configuration B. **(d)** Both the STA/LTA and the polarization detector miss Sn and pick the secondary Sg phase.

configuration of the search windows, even if tS_{pre} is used as t_{AC}. For distances less than Δ_{AIC_3}, we extend the search windows in a way that includes possible triggers from the detectors.
At distances above Δ_{AIC_3} we expect Sn as the first arriving S-phase and the maximum STA/LTA value $tS2L_{max}$ is usually associated with the arrival of a later (impulsive) phase (Sg or SmS). To avoid phase misidentification as described in Figure S5, the AR-AIC windows are adjusted in a way such that $tS2L_{max} - t_{SE} > 0$. In analogy to P-phase picking for same earthquakes (*Diehl et al.*, 2009) we choose $\Delta_{AIC_3} = 100$ km. Furthermore, picks are rejected if the minimum AIC is located close to the start or the end of the picking window for several components. A minimum AIC close to the edge of the picking window is usually an indicator for misconfigured AR-AIC search windows.

B.4 Quality Assessment in Combined Approach

Robust uncertainty estimates for automatic S-arrivals can be obtained by combining picking information from different techniques to define lower tS_{lo} and upper tS_{up} limit of the error interval. The mean position of this interval $tS_{me} = (tS_{up} + tS_{lo})/2$ is defined as the S-arrival time. In our approach, the earliest and latest possible pick from the STA/LTA detector (tS_{min1}, tS_{thr1}), polarization detector (tS_{min2}, tS_{thr2}), and the different AIC minima (tS_{AC}, with $C = N, E, Q, T, H$) constitute the lower and upper limits of the corresponding error interval.
In addition, the width of the AIC minimum is usually related to the quality of the onset. Impulsive wavelets like the S-arrival on the T component in Figure 4 lead to a distinct AIC minimum, whereas emergent wavelets produce broader minima (Fig. S5c). The width of the AIC minimum can therefore be used as an additional quality information about the arrival time and is also a good indicator for the presence of possible precursory phases. We define the earliest possible arrival derived from the AIC function as the first sample where AIC drops below thr_{AIC} and the latest possible arrival as the last sample below thr_{AIC} (see Fig. 4 and S5c). If AIC_{min} represents the minimum and AIC_{max} the maximum AIC value within the picking window, thr_{AIC} is defined as 10% of the differential AIC:

$$thr_{AIC} = AIC_{min} + (AIC_{max} - AIC_{min})/10 \tag{S16}$$

The dashed horizontal lines in Figure 4 and S5b,c denote the threshold thr_{AIC} for the AIC-quality assessment. The corresponding positions of 'earliest-possible' and 'latest-possible' arrivals are represented by tS_{eT}, tS_{eQ}, tS_{lT}, and tS_{lQ}. The usage of the AIC-quality assessment becomes especially important for appropriate uncertainty estimates at larger epicentral distances. In the following, we define the distance Δ_{AIC_2} above which the AIC quality assessment is considered for the overall quality assessment.

Quality Weighting Scenarios

Since detectors and components are sensitive to different phase types in different distance ranges, we setup four different weighting scenarios derived from the calibration with the reference data set. The weighting scenarios are also summarized in Table 2.

Scenario 1: S-phase recognized by polarization detector at distances $\Delta_{epi} < \Delta_{AIC_3}$ (Sg dominated range)

The polarization detector represents the best indicator for a pure S-wave arrival. In case of a detection, we use the polarization picks tS_{thr2}, tS_{min2}, and the combined AR-AIC minimum tS_{AH} to derive the uncertainty interval. Furthermore, we consider the AR-AIC picks derived on rotated components (T or Q). Due to the radiation pattern and observation azimuth, the energy of the S-wave can be distributed unevenly between T and Q. Therefore, the S-onset might be of a different quality on different components (see Fig. S3). In addition, the T component should be less affected by potential Sp energy. To avoid unrealistic large error intervals, we consider only the component, whose AR-AIC minimum tS_{AC} is closest to the S-wave detection tS_{min2}. For epicentral distances above Δ_{AIC_2}, additional information provided by tS_{eH} and tS_{eT} or tS_{eQ} is used for error interval determination. Finally, we calculate the average pick position tS_{av}, standard deviation σ_{pk}, earliest pick position tS_{er}, and latest pick position tS_{la} from the provided picks. To account for possible precursory S-phases tS_{er} represents always the position of the lower error interval tS_{lo}. The upper error interval is derived from $tS_{up} = tS_{av} + \sigma_{pk}$.

Scenario 2: S-phase recognized only by STA/LTA detector at distances $\Delta_{epi} < \Delta_{AIC_3}$ (Sg dominated range)

In this case, the phase type is likely to be less well constrained. Besides tS_{thr1} and tS_{min1}, AR-AIC minimum picks tS_{AC} from all components (N, E, Q, T, H) are considered for determination of tS_{lo} and tS_{up}. For epicentral distances above Δ_{AIC_2}, additional information provided by tS_{eC} is considered for error interval determination. Again, tS_{er} represents the position of the lower error interval tS_{lo} and the upper error interval is derived from $tS_{up} = tS_{av}$.

Scenario 3: S-phase recognized by polarization or STA/LTA detector at distances $\Delta_{epi} \geq \Delta_{AIC_3}$ (Sn dominated range)

In the distance range around the crossover between Sg to Sn as the first arriving S-phase, arrivals picked by STA/LTA and polarization detectors are often associated with impulsive later phases. In this scenario the error assessment is solely based on the uncertainty estimates obtained from the AIC function. We calculate the mean and standard deviation from tS_{eC}, tS_{AC}, tS_{lC}, with $C = N, E, Q, T, H$. The mean position of the S-wave is represented by the average picking position, the error interval is defined by $\pm\sigma_{pk}$.

Scenario 4: S-phase recognized neither by polarization nor STA/LTA detector (at all distance ranges)
The phase type picked by the AR-AIC picker is rather unreliable. The phase is rejected by default.

The error interval is used to calculate the mean position of the S-wave arrival and to assign a discrete quality class according to an *a priori* user defined weighting scheme.
Finally, a minimum amplitude signal-to-noise ratio $S2N_{min}(m)$ is defined for each quality class m. If the signal-to-noise ratio of the current pick is less then $S2N_{min}(m)$, the pick is downgraded to the next lower quality class and its signal-to-noise ratio is checked again for the new class. Since we expect smaller signal-to-noise ratios for potential Sn phases, we define different sets of $S2N_{min}(m)$ above and below Δ_{AIC_3}. Figure 5 and S6 show examples for different automatic S-wave arrival picks and their corresponding error intervals at distances dominated by Sg and Sn, respectively. The mean position and the

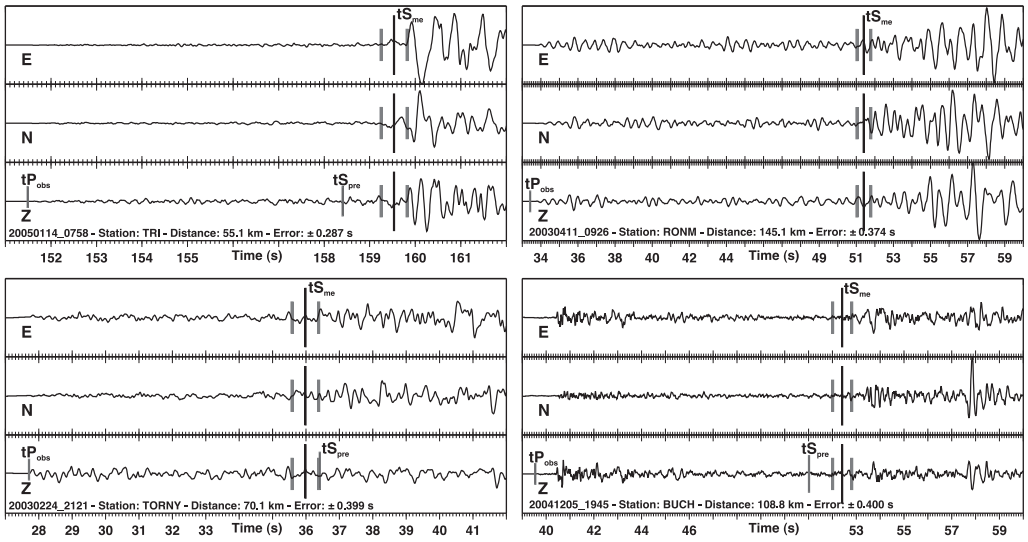

Figure S6: Further examples of automatic S-wave picks at epicentral distances dominated by first arriving Sg phases (left column) and first arriving Sn phases (right column) for different error intervals. The error interval derived from the automatic quality assessment is represented by the vertical gray bars. The vertical long black bars denote the mean position of the S-wave onset. Error interval and mean position agree very well with the actual S-wave arrival observed on the seismograms.

error intervals of the automatic picks agree very well with the actual S-wave arrival observed on the seismograms.

C Application to Alpine Region (Supplementary Material)

C.1 Average Picking Uncertainty

The average picking uncertainty of an arrival-time data set can be estimated from the number of picks and the uncertainty interval of each class. Assuming L quality weighting classes i ($i = 1, \ldots, L$), each class is associated with an uncertainty interval ε_i. The number of picks of the ith class is described by N_i. The average picking uncertainty can be estimated from:

$$\varepsilon_{avr} = \frac{1}{\sum_{i=1}^{L} N_i} \sum_{i=1}^{L} \varepsilon_i N_i \tag{S17}$$

C.2 Picking Performance for Tomography

Table 3 and 5 demonstrate that some S-waves can be picked in principle with an accuracy $\leq$ 100 ms by hand as well as by our automatic algorithm. On the other hand, the highest quality '0' is the less populated class and most of the reference as well as automatic S-picks are classified as '1'. Such an unbalanced distribution of errors indicates an optimistic weighting scheme, which is not appropriate for seismic tomography. Since we are usually interested in an uniform ray-coverage (resolution) in 3-D tomography, we are not able to benefit from a minority of high-accurate observations if the majority of data is of a lower quality. On the other hand, the minimum velocity perturbation resolvable depends on data error and on model parametrization. Due to this trade-off, an appropriate parametrization turns out to be rather difficult for such a weighting scheme.
To obtain an appropriate weighting scheme for seismic tomography, we merge class '0' and '1'. The simplified weighting scheme contains only two usable ('0' and '1') and one reject class ('2') as illustrated in Table S3. The highest quality represents the largest populated class, and the average picking error of the training-mode adds up to about 0.29 s in this new weighting scheme (only slightly higher than the average error in the original weighting scheme). Such a well-balanced weighting scheme facilitates the model parametrization for tomography. On the other hand, the weighting scheme of Table 5 is rather suitable for earthquake location problems, since single high-quality S-arrivals can significantly reduce the uncertainty of the hypocenter determination.

C.3 Parameter Search Procedure

To derive a satisfactory picker-performance for a certain data set, appropriate values of the parameters listed in Tables 4 and S4 have to be evaluated from a trial-and-error procedure. The picker is applied to the reference data for each

Reference Quality Classification	Automatic Quality Classification 0	1	2 (rej)	Σ Ref
0	N_{00} = 142 33 % σ_{00} = 0.10 s	N_{01} = 102 24 % σ_{01} = 0.31 s	N_{02} = 189 43 % σ_{02} = 1.22 s	N_0^{Ref} = 433 $\lvert\varepsilon_0\rvert \le 0.2$ s
1	N_{10} = 13 7 % σ_{10} = 0.17 s	N_{11} = 35 20 % σ_{11} = 0.33 s	N_{12} = 128 73 % σ_{12} = 1.60 s	N_1^{Ref} = 176 $\lvert\varepsilon_1\rvert \le 0.4$ s
2 (rej)	**N_{20} = 0** **0 %** **σ_{20} = 0.00 s**	N_{21} = 2 1 % σ_{21} = Not av.	N_{22} = 186 99 % σ_{22} = 0.69 s	N_2^{Ref} = 188 $\lvert\varepsilon_2\rvert < 0.4$ s
Σ Aut	N_0^{Aut} = 155 σ_0 = 0.12 s $\overline{\Delta AR}_0$ = -0.01 s	N_1^{Aut} = 139 σ_1 = 0.31 s $\overline{\Delta AR}_1$ = 0.11 s	N_2^{Aut} = 503	

Table S3: Performance of the automatic S-wave picker for simplified weighting scheme (3 quality classes) in matrix presentation as in Table 5.

set of parameters and its resulting performance has to be assessed as described in the body of the article. Guidelines on how the critical parameters have to be evaluated for a certain data set are provided in the body of the article. In this section we give additional information on less critical parameters of Table S4, which were not discussed in the body of the article.

- ΔS_{post}: Has to be evaluated from the maximum deviation between predicted arrivals (depending on accuracy of velocity model) and reference picks. The value should be large enough to guarantee that the coarse S-window includes the actual arrival of the S-phase.

- ΔP_{gap}: The length of the safety gap between tP_{obs} and $SW1$ depends on the width of the P-wave signature present in the STA/LTA characteristic function and on the minimum epicentral distance. In principle, a value of 0.75 s would confine the minimum epicentral distance to about 5 to 6 km (for shallow earthquakes). In practice, its value is less critical, since the polarization-detector is pretty reliable for close-by events and in this case, the STA/LTA detector is not considered at all. It might have to be adjusted for special studies such as microseismicity.

- *tdw* of STA/LTA detector: Due to the rather smooth shape of the characteristic function of the STA/LTA detector, *tdw* does not have to account for singularities and can be set to zero. If Δst and Δlt are adjusted to higher resolution, we expect a more complicated characteristic function and it might be necessary to choose a value > 0.

- n: Controls the effect of absolute amplitude weighting of CF_S. A value of 0 disables the weighting (CF_S corresponds to the orginal definition of *Cichowicz* 1993). Using a value of 0 lead to several false detection (noise) in our application. A high value of e.g. 1.0 could lead to missed Sn arrivals. A value of 0.5 represents the best compromise for our data set.

- $M(1), M(2)$: The maximum order of the AR-model has not much effect on the AR-AIC performance due to the AR-modeling method implemented in our approach (see *Takanami and Kitagawa* 1988 for details). A value between 10 and 20 is appropriate.

- κ^1_{min},κ^1_{max}: Minimum and maximum v_P/v_S ratio expected in a region for phases sampling mainly the upper crust. Can be used to identify gross mispicks, similar to the use of Wadati diagrams. Usually, we expect values between 1.5 and 2.1.

- κ^2_{min},κ^2_{max}: Minimum and maximum v_P/v_S ratio expected in a region for phases sampling mainly the lower crust. Here we expect a narrower band of v_P/v_S ratios.

- Waveform Filters: Performance of the picker should be checked for different frequency bands. Based on experience from routine and reference picking, the Wood-Anderson filter facilitates identification of S-wave arrivals. This observation is confirmed by the behavior of the automatic picker, since we obtained the best performance with the application of the Wood-Anderson filter.

Parameter	Description	Value
General Parameters		
ΔS_{post}	Defines upper end of coarse S-wave search window	5 s
Parameters for STA/LTA Detector		
ΔP_{gap}	Safety gap between tP_{obs} and $SW1$	0.75 s
tdw	Maximum time CF drops below threshold	0.00 s
Parameters for Polarization Detector		
n	Exponent for absolute amplitude weighting of CF_S	0.5
Parameters for AR-AIC Picker		
$M(1)$	Maximum order of AR-model (noise)	15
$M(2)$	Maximum order of AR-model (signal)	15
Parameters for Quality Assessment		
κ^1_{min}	Minimum v_P/v_S ratio defining S-window ($\Delta_{epi} < \Delta_{AIC_3}$)	1.500
κ^1_{max}	Maximum v_P/v_S ratio defining S-window ($\Delta_{epi} < \Delta_{AIC_3}$)	2.050
κ^2_{min}	Minimum v_P/v_S ratio defining S-window ($\Delta_{epi} \geq \Delta_{AIC_3}$)	1.600
κ^2_{max}	Maximum v_P/v_S ratio defining S-window ($\Delta_{epi} \geq \Delta_{AIC_3}$)	1.825
Waveform Filters		
$\Delta_{epi} < \Delta_{AIC_3}$: Wood-Anderson		
$\Delta_{epi} \geq \Delta_{AIC_3}$: Wood-Anderson + additional 0.5 Hz HP-filter		

Table S4: Additional parameters which have to be adjusted for the described picking approach. The suggested values are derived from a parameter search comparing automatic picks with reference picks of local earthquakes within the greater Alpine region.

D Outlier Detection (Supplementary Material)

D.1 Outlier-Detection in Test-Mode

To assess the performance of the automatic picker especially in terms of systematic mispicks and outliers present in the test-mode, we display the difference between automatic and reference S-picks (ΔAR) for usable automatic picks against epicentral distance in Figure 7. In general, the number of outliers is low and the corresponding errors are rather large. The number of gross outliers increases in the distance range of the triplication zone (Fig. 7). Here, the first arriving weak Sn phases are usually followed by an impulsive Sg and the AR-AIC picker can fail to discriminate the two phases, even if a dynamic adjustment of search windows is applied (example $e1$ in Fig. 7). Since we use the picks provided by the detectors to setup the AR-AIC windows for smaller epicentral distances, false detection can also result in the wrong phase identification for some Sg phases, as marked by example $e2$ in Figure S5. Here, the polarization detector triggers at a later arriving phase due to the small degree of linear polarization of the preceding earlier phase picked as reference S-arrival.

If the automatic picker is applied to a data set without reference picks (production-mode) we have different possibilities to identify possible outliers. A common way to detect mispicked S-arrivals is the usage of Wadati diagrams as described, for example, by *Kisslinger and Engdahl* (1973) or *Maurer and Kradolfer* (1996). In Figure S7a we plot $\Delta_{SP} = tS_{me} - tP_{obs}$ against the P-wave travel time $\Delta_P = tP_{obs} - t_0$ for individual (usable) automatic S-picks from the training-mode. For a comparison between automatic and reference S-picks we use the same origin time t_0 as provided by the P-wave minimum 1-D location and compute the corresponding average v_P/v_S ratios at different distance ranges (0-50 km, 50-100 km, 100-150 km) similar to Wadati diagrams. The corresponding result for the reference S-picks is presented in Figure S7b. The average v_P/v_S ratios show no significant systematic bias between automatic and reference S-picks.

The positions of 'automatic' mispicks $e1$ and $e2$ are marked as black bold crosses in Figure S7a. Example $e2$ indicates a rather high v_P/v_S ratio close to 2.0. Although wrong by more than one second, $e1$ cannot be identified explicitly as an outlier pick.

An increased scatter among the reference picks can be observed in Figure S7b. Especially at larger distances several obvious outliers are present in the reference data. In case of example $e3$, the weak earlier Sn phase was not recognized in the reference hand picking and the later-arrival phase was misinterpreted as the first arriving S-wave, which leads to an error of several seconds. The automatic pick for the same recording was rejected by the automatic quality assessment and is therefore not included in Figure S7a. This example demonstrates the difficulty and ambiguity in manually picking and identification of S-waves, especially beyond the cross-over distance between Sn and Sg. On

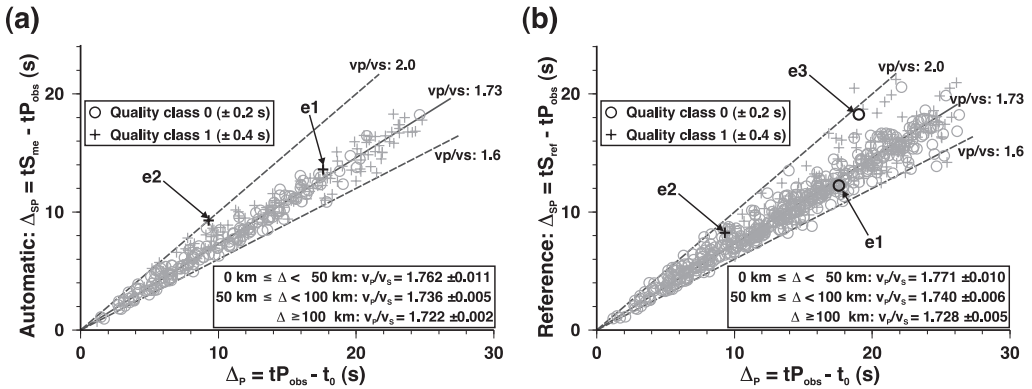

Figure S7: Modified Wadati diagrams based on **(a)** automatic S-picks from the training-mode and **(b)** reference S-picks. The fixed origin times t_0 are provided by the P-wave minimum 1-D locations. Dashed lines denote range of extreme v_P/v_S ratios of 2.0 and 1.6. Solid line represents theoretical v_P/v_S of 1.73 expected for a Poisson solid. Average v_P/v_S ratios derived from automatic and reference picks for three different distances ranges are given in the boxes. Example outliers $e1$, $e2$, and $e3$ as discussed in the text are marked by black symbols.

the other hand, the more conservative quality assessment of the automatic approach significantly reduces the scatter in S-phase arrivals (Fig. S7a) at the cost of a lower number of usable picks.

D.2 Outlier-Detection in Production-Mode

The production-mode yields 1618 class '0' (± 0.2 s) and 973 class '1' (± 0.4 s) automatic picks. Hence, 57% of the (non-clipped) potential S-phases could be picked with our approach. If outliers are disregarded, the average picking error adds up to about 0.27 s. Since outliers are associated with errors up to several seconds, they lower the average accuracy of the automatic picks significantly. Therefore, outliers have to be identified and removed from the data set.
As for the test-mode, we derived average v_P/v_S ratios from modified Wadati diagrams. The results for the three distance ranges agree very well with the values derived from reference S-picks (Fig. S7b), which suggests that performance of the production-mode is comparable with the test-mode. As demonstrated for the test-mode, the analysis of individual $S-P$ versus P-wave travel times is not sufficient to detect moderate outliers in the production-mode. Therefore, all automatic S-picks indicating $v_P/v_S > 1.75$ were cross-checked against waveforms for distances > 50 km in a semi-automatic procedure to assess the number of outliers due to misinterpreted phases. From 450 analyzed automatic picks, 42 (9%) were identified as obvious mispicks or highly questionable automatic picks. Most of these mispicks resulted from phase misinterpretation analogous to example $e1$ in Figure S7 in the distance range of the triplication zone (90-110 km). The 42 clearly identified mispicks represent about 2% of all automatic picks.

References

Akazawa, T. (2004), A technique for automatic detection of onset time of P- and S-phases in strong motion records, in *13th World Conference on Earthquake Engineering*, Vancouver, Canada, paper No. 786.

Baer, M., and U. Kradolfer (1987), An automatic phase picker for local and teleseismic events, *Bull. Seism. Soc. Am.*, *77*, 1437–1445.

Cichowicz, A. (1993), An automatic S-phase picker, *Bull. Seism. Soc. Am.*, *83*, 180–189.

Crampin, S., and J. H. Lovell (1991), A decade of shear-wave splitting in the Earth's crust: What does it mean? What use can we make of it? And what should we do next?, *Geophys. J. Int.*, *107*, 387–407.

Diehl, T., E. Kissling, S. Husen, and F. Aldersons (2009), Consistent phase picking for regional tomography models: Application to the greater Alpine region, *Geophys. J. Int.*, *176*, 542–554, doi:10.1111/j.1365-246X.2008.03985.x.

Fuchs, K., and G. Müller (1971), Computation of synthetic seismograms with the reflectivity method and comparison with observations, *Geophys. J. Roy. Astron. Soc.*, *23*, 417–433.

Kisslinger, C., and E. R. Engdahl (1973), The interpretation of the Wadati diagram with relaxed assumptions, *Bull. Seism. Soc. Am.*, *63*, 1723–1736.

Maurer, H., and U. Kradolfer (1996), Hypocentral parameters and velocity estimation in the western Swiss Alps by simultaneous inversion of P- and S-wave data, *Bull. Seismol. Soc. Am.*, *86*, 32–42.

Plešinger, A., M. Hellweg, and D. Seidl (1986), Interactive high-resolution polarization analysis of broad-band seismograms, *J. Geophys.*, *59*, 129–139.

Samson, J. C. (1977), Matrix and stokes vector representations of detectors for polarized waveforms: theory, with some applications to teleseismic waves, *Geophys. J. R. Astr. Soc.*, *51*, 583–603.

Sleeman, R., and T. van Eck (1999), Robust automatic P-phase picking: an on-line implementation in the analysis of broadband seismogram recordings, *Phys. Earth Planet. Inter.*, *113*, 265–275.

Takanami, T., and G. Kitagawa (1988), A new efficient procedure for the estimation of onset times of seismic waves, *J. Phys. Earth*, *36*, 267–290.

Thurber, C. H., and S. R. Atre (1993), Three-dimensional v_p/v_s variations along the Loma Prieta rupture zone, *Bull. Seism. Soc. Am.*, *83*, 717–736.

Weiss, T., S. Siegesmund, W. Rabbel, T. Bohlen, and M. Pohl (1999), Seismic velocities and anisotropy of the lower continental crust: A review, *Pure Appl. Geophys.*, *156*, 97–122.